Materials Advances

ROYAL SOCIETY OF CHEMISTRY

PAPER

View Article Online
View Journal | View Issue

Cite this: *Mater. Adv.*, 2024, 5, 1240

Highly conductive biocarbon nanostructures from burlap waste as sustainable additives for supercapacitor electrodes†

Haftom Weldekidan, [ab] Singaravelu Vivekanandhan, [c] Neelima Tripathi, [ab] Amar Mohanty *[ab] and Manjusri Misra [ab]

Received 1st August 2023,
Accepted 25th November 2023

DOI: 10.1039/d3ma00491k

rsc.li/materials-advances

Biocarbon materials with high electrical conductivity have received great attention in many applications such as energy storage/conversion, EMI shielding and electrical/electronic components. We have successfully synthesized biocarbon nanostructures from waste burlap using a two-step thermochemical conversion process involving carbonization at 600 °C followed by graphitization at 1200 °C with an iron nitrate catalyst. The resulting material exhibited an extremely high electrical conductivity of 375 S m^{-1}, which is 15 times higher than those of commercial-grade graphene and carbon black. The high electrical conductivity was mainly due to the formation of a few layers (3–12) of graphene nanosheets with relatively uniform particle morphology and pore size distributions. Owing to its superior electrical conductivity, the waste burlap derived biocarbon nanostructure was effectively used as a sustainable conductive additive in the fabrication of electrodes for electrical double layer capacitors (EDLCs), which exhibited excellent performance compared to the commercial carbon black (SP) and commercial-grade graphene (CG). This work can open up exciting prospects to address the demand for sustainable alternatives to the conventional fossil-based materials in a wide range of cutting-edge applications.

1. Introduction

Electrical conductivity is one of the most demanding properties of carbon materials due to their potential applications in conductive composites, electrodes for energy storage devices, electromagnetic interference (EMI) shielding, and sensing/switching/electronic devices.[1,2] Hence, carbon black, carbon nanotubes, carbon nanofibers and graphene have garnered considerable importance in materials science due to their higher electrical conductivity. Among them, carbon black, which is one of the widely used fossil-based carbon materials, has excellent thermal and electrical conductivities, but still has serious problems from environmental, sustainability and climate change perspectives. Recent advancement in the field of carbon materials is their production from various renewable resources. More attention is being paid to the synthesis of a wide range of carbon nanostructures from renewable resources due to their unique properties in the nano-regime. Conversion of biomass materials into biocarbon nanostructures is one of the key strategies of sustainable manufacturing, which reduces the global dependency on fossil resources for a wide range of carbon allotropes with diverse physicochemical properties. Achieving high electrical conductivity (comparable to conventional carbon materials) in biocarbon materials is still a challenging task, which hampers their potential for diverse applications.

Electrical conductivity of biocarbon materials mainly depends on their graphitic nature, which is influenced by many factors such as the properties of feedstock and pyrolysis temperature.[3] Pyrolysis is a thermochemical process in which organic materials are subjected to high temperature treatment in the absence of oxygen. Specifically, in the context of biocarbons, the precursors, which may include biomass or organic waste materials, undergo a series of complex decomposition reactions during pyrolysis which involve dehydration, depolymerization, and the generation of volatile compounds, ultimately resulting in the formation of biocarbons.[4,5] In most of the cases, pyrolysis temperature affects the electrical conductivity of biocarbons as graphitic carbons with highly crystalline structures are formed at higher pyrolysis temperatures. In addition, the electrical conductivity of biocarbons is affected by the hydrogen to carbon and oxygen to carbon ratios. It was noticed that a decrease in C-to-H and O-to-C ratios increased the electrical conductivity of

[a] *Bioproducts Discovery and Development Centre, Department of Plant Agriculture, Crop Science Building, University of Guelph, Guelph, N1G 2W1 Ontario, Canada. E-mail: mohanty@uoguelph.ca*
[b] *School of Engineering, University of Guelph, Guelph, N1G 2W1 Ontario, Canada*
[c] *Sustainable Materials and Nanotechnology Lab, Department of Physics, V. H. N. S. N. College (Autonomous), Virudhunagar, 626 001, Tamil Nadu, India*

† Electronic supplementary information (ESI) available. See DOI: https://doi.org/10.1039/d3ma00491k

biocarbon materials,[6] which are highly influenced by the pyrolysis temperature.[7] Additionally, changes in physical characteristics, such as the surface area, metal content, and pore size distribution, have considerable impacts on electrical conductivity.[8]

Biomass materials can be converted to highly structured carbons with superior electrical conductivity at high pyrolysis temperatures. Demir *et al.*[9] synthesized highly graphitic biocarbon by employing metal-catalyzed hydrothermal carbonization (HTC) following graphitization at 1100 °C. The hydrothermal carbonization increases the carbon content of the sample and eliminates volatiles, while the high-temperature treatment promotes the formation of graphitized carbons with better electrical conductivity in the range of 10.6 S m^{-1}.[9] Similarly, Kane *et al.*[10] reported high electrical conductivity (1850 S m^{-1}) for lignin-derived graphitic carbons produced at 1100 °C, when packed to the 0.5 packing fraction. Besides temperature, catalysts influence the degree of graphitization during biomass pyrolysis. High quality graphitic carbon was produced by the pyrolysis of lignin at 1100 °C using catalysts $Co(NO_3)_2$ and $Fe(NO_3)_3$, which improved the single particle electrical conductivity of the carbon from 1 to 10.6 S m^{-1}.[9] Similarly, the biocarbon produced from lignin at 1000 °C using the $Mn(NO_3)_2$ catalyst showed improved conductivity (11 S m^{-1}) and thermal stability due to its high graphene content.[9] In addition to the graphitic nature and chemical makeup, the packing fraction also affects the electrical conductivity of biocarbons by improving the surface contact.[11–14]

Biocarbon materials have been extensively explored as the active electrode materials for supercapacitors due to their electrical conductivity, structural stability, higher specific surface area, and surface functionality, showing comparable specific capacity to the conventional fossil resource-based carbon materials.[15–17] However, they have not been used as the conductive additives (which are used up to 10% of the electrode composition) due to their inadequate electrical conductivity. Recently, Kane *et al.*[18] reported effective utilization of biochar as a renewable substitute for commercial carbon black due to its higher electrical conductivity for the fabrication of electrodes for Li ion batteries. Biocarbons made from biomass materials can exhibit superior features compared to the carbon black, not only in terms of green and sustainability perspectives but also in terms of their high electrical conductivities. As the concern about the sustainability of electric vehicles (EVs) increases, there is a demand for reducing the usage of fossil-based materials in their supply chains, including structural components and energy storage devices. Utilizing the developed biocarbon nanostructures as the sustainable conductive additives in energy storage devices is expected to revolutionize the EV industry towards green[19] technologies.

To the best of our knowledge, biocarbon materials have not been explored as the conductive additives for the fabrication of EDLC electrodes. In this work, burlap waste was effectively converted to highly conductive biocarbon nanostructures *via* two-step catalytic pyrolysis, and then explored as efficient substitute for the conventional conductive carbon in the fabrication of EDLC electrodes. The obtained biocarbons were characterized by high-resolution transmission electron microscopy (HRTEM), X-ray diffraction (XRD), Raman, and scanning electron microscopy with energy dispersive X-ray spectroscopy (SEM–EDX) techniques to understand the relationship between their physicochemical properties and their electrical conductivity.

2. Methods

2.1. Materials and biocarbon synthesis methods

Commercial grade graphene nanoplatelets (CAS: 7782-42-5) (hereinafter called CG) having a surface area of 500 m^2 g^{-1} were purchased from Fisher Scientific and carbon black Super P C65 (SP hereinafter) was purchased from Timcal Ltd. Iron(III) nitrate nonahydrate ($Fe(NO_3)_3{\cdot}9H_2O$, 99.95% purity) was purchased from Sigma-Aldrich. Supercapacitor electrodes were prepared using 0.2 mm thick 304 grade stainless steel sheets supplied by Sun Metals, Madurai, Tamil Nadu, India. Polyvinylidene fluoride (PVDF) was used as the binder, which was obtained from Alfa Aesar, India. In addition, *N*-methyl-2-pyrrolidone (NMP) solvent was procured from Hi-Media, India. All the chemicals were used in this research without any purification or modification.

Waste burlap bags were chopped and dried in an oven at 80 °C for 24 hours and then pyrolyzed in the Carbolite Gero pyrolyzer (GLO 10/11-1G) at 600 °C, 5 °C min^{-1}. Once the temperature dropped to the ambient, the carbonized material (BC6 hereinafter) was ball milled for an hour with a Fritsch Pulverisette 5 (Germany) and sieved through a 1 mm mesh size. To prepare the graphitized biocarbon (GB12 hereinafter), the obtained BC6 was mixed with 10 wt% aqueous solution of iron(III) nitrate nonahydrate ($Fe(NO_3)_3{\cdot}9H_2O$) by keeping the ratio of the catalyst to BC6 as 1 : 49. Furthermore, the mixture was stirred for three hours with a magnetic stirrer and heated to 80 °C and then kept in an oven at 105 °C for 24 hours to remove the moisture. The dried mixture was subsequently graphitized in the 1610 FL Laboratory Box Furnace at 1200 °C, ramping at 20 °C min^{-1} under a flowing N_2 gas atmosphere.

2.2. Characterization

The elemental analysis of the biocarbons was performed using a CHNS analyzer from Thermo Fisher Scientific (Waltham, USA), while the oxygen content was calculated by difference. The biocarbons were further analysed using inductively coupled plasma optical emission spectroscopy (ICP-OES) to estimate metallic iron concentration.

The specific surface area and pore size distributions of the carbons were determined from nitrogen adsorption isotherms measured at (−196 °C) using the Autosorb-iQ analyser (Quantachrome Instruments, USA). Around 200 mg of the samples were first degassed at 200 °C for 3 hours and then subjected to nitrogen adsorption/desorption cycles at relative pressures between 0.02 and 0.99. For the BET surface area, the results were fitted to the Brunauer–Emmett–Teller (BET) model, whereas the pore size distribution was obtained using the

density functional theory (DFT) model incorporated in the AsiQwin software.

Powder XRD was performed using a PANalytical Empyrean diffractometer with a reflection (Bragg–Brentano) geometry having a Cu Kα radiation source, Ni Kβ filter, and PIXcel1D linear detector. The diffraction pattern was recorded at room temperature at 2θ values between 5° and 80° with a step size of 0.0131° and an exposure time of 90 seconds per step. Data collection was performed using HighScore Plus (version 4.1).[20]

Raman spectra of the biocarbon materials were acquired using the DXR2 Raman microscope from Thermo Fisher Scientific. The aperture pinhole was set to 50 micrometers, while the laser power and wavelength were set at 3 mW and 532 nanometers, respectively.

Morphological features of the biocarbon samples were investigated using the Phenom ProX SEM. Samples were first dispersed on a conductive carbon support mounted on an aluminum stub and then placed in the SEM. The images were recorded employing the electron beam with the accelerating voltage of 10 kV.

High-resolution nanoscopic images of the biocarbon materials were obtained using a Thermo Scientific Talos 200 HRTEM, operated with the electron beam of 200 kV.

2.3. Electrical conductivity measurements

Electrical conductivity of the biocarbon materials was estimated from the bulk electrical resistance measured using the Autolab PGSTAT302N potentiostat attached to an FRA32 M module and an AUTO 85394 differential electrometer-amplifier (Metrohm Autolab, Utrecht, Netherlands). A sample of around 250 mg was placed between two aluminium pistons and contained in a clear plastic tube (Fig. S1, ESI†). The measurement was performed by applying 10 mV over a frequency range of 400 to 600 kHz with the increasing loads of 1, 3, 5, 7 and 9 kg on the piston.[11,21] Five different sets of resistivity measurements, each repeated at least three times, were performed for each load. The electrical conductivity (σ) was then determined from eqn (1):

$$\sigma = h/AR \quad (1)$$

where h is the height of the packed sample (cm), which was obtained by measuring the displacement between the initial and final heights, A is the base area of the tube (cm^2) and R represents the measured electrical resistance (Ω).

2.4. Supercapacitor studies

2.4.1. Fabrication of supercapacitors. The burlap waste derived biocarbon nanostructures were effectively utilized to substitute the commercial conductive carbon black (Super P C65 (SP)) as the additives in electrode fabrication for supercapacitor applications. The supercapacitor electrode was fabricated by using (i) a seaweed derived pristine biocarbon (PC) material as the active material, (ii) Super P C65 (SP), biocarbon nanostructures (GB12) and commercial graphene (CG) as conductive additives, and (iii) PVDF as a binder respectively with a weight proportion of 80 : 10 : 10 (160 mg : 20 mg : 20 mg). The electrode was also fabricated without any conductive additives for the purpose of comparison with 90% (180 mg) of the active material and 10% (20 mg) of the binder. The mixture of active materials, conductive additives and the binder was made into a homogeneous slurry using NMP by mechanical grinding using an agate mortar and pestle. Furthermore, the slurry was coated on the surface etched flag shaped stainless steel (SS) sheet with an electrode surface area of 4 cm^2 (2 × 2) and dried in a hot air oven at 80 °C for 12 hours followed by hydrolytic pressing at 1 ton. The mass loadings of the electrodes are 13 mg, 14 mg, 8 mg and 8 mg respectively for the electrodes of PC, PC+SP, PC+GB12 and PC+CG. The fabricated electrodes were assembled into supercapacitor cells adopting pouch cell assembly using a PP pouch (3 × 4 cm), Whatman filter paper (No. 1) as a separator and 1 M KOH as an electrolyte. The fabricated pouch cell was compacted with the PP blocks (4 × 4 cm) to avoid the movement of electrodes during the electrochemical testing process.

2.4.2. Electrochemical characterization. The electrochemical characteristics of the fabricated capacitive cells were investigated using an electrochemical workstation, an SP-200 potentiostat from Bio-Logic, France, by means of cyclic voltammetry (CV), galvanostatic charge–discharge (GCD) and electrochemical impedance spectroscopy (EIS) studies. CV was performed by varying the scan rates from 20 to 180 mV s^{-1} in steps of 20 mV s^{-1} and the specific capacitance calculated from the obtained CV curve is given by the formula,

$$C_s = \frac{4}{mv\Delta E}\int i\,dV \quad (2)$$

where the integral component represents the area of the discharge curve, v is the scan rate (mV s^{-1}), ΔE is the fixed voltage range (V), and m is the total mass of the active material (g).

Electrochemical impedance of the fabricated capacitive cells was recorded in the frequency window of 100 kHz–100 MHz at 10 mV before and after 5000 cycles. The galvanostatic charge–discharge studies of the fabricated capacitive cells were conducted by applying a current density from 0.5 to 5 A g^{-1}, in steps of 0.5 A g^{-1}. GCD profiles were effectively used to estimate the specific capacitance of the electrodes through the following equation.[22,23]

$$C_s = \frac{4i}{m(dV/dt)} \quad (3)$$

where i is the discharge current (A), m is the total mass of the active material (g), dV is the discharge potential window (V), and dt is the corresponding discharge time (s). In addition, other key parameters of the supercapacitors are power and energy densities, which can be calculated using the results of GCD studies employing the following formulas,

$$E = \frac{1}{2}\times\frac{1}{4}\times\frac{1}{3.6}\times C_s\times(dV)^2 \quad (4)$$

$$P = \frac{E\times 3600}{dt} \quad (5)$$

In expression (4) the "4" in denominator is the conversion factor

of the electrode to the total cell and "3.6" is used for the unit conversion (J g^{-1} to Wh kg^{-1}). The cycle performance of the fabricated capacitive cells was recorded up to 5000 cycles to understand their capacitance retention.

3. Results

3.1. Elemental composition of biocarbons

Increasing the pyrolysis temperature increased the carbon content of the biocarbons, and the oxygen content was observed to decrease from 31% to 6.5% with temperature (Table 1). The carbon content of the burlap carbon produced at 600 °C (BC6) is only 63 wt% but substantially increased to 93 wt% when catalyzed by iron nitrate at 1200 °C. The oxygen to carbon ratio has significantly reduced from 0.5 to 0.069 by increasing the pyrolysis temperature from 600 to 1200 °C. The removal of oxygen with increasing temperature is expected to lead to the formation of more graphitic carbons, hence improving the conductivity.[14] The presence of more oxygen in biocarbon materials distorts the graphitic structure and increases the sp^3 hybridized carbons (defect carbons) in the structure, which can affect the electron flow within the particles.[6] Besides, the loss of hydrogen due to the higher pyrolysis temperature can increase the quality of the graphitic structure present in the biocarbon nanostructure.

ICP-OES was used to examine the concentration of iron in both the samples, BC6 and GB12, which was found to be only 0.14% for GB12 and 0.053% for BC6. Since iron nitrate was used in the preparation of catalysts, its presence in GB12 indicated that traces of iron remained in the sample after graphitization, but not significantly high enough to impact its conductivity. The properties of biocarbons, including electrical conductivity, are less affected by metallic concentrations below 15%.[24]

3.2. Physicochemical characterization of biocarbon nanostructures

3.2.1. Morphology and nanoscopic investigation. The morphological structure of the biocarbons is substantially influenced by the temperature and catalyst treatment. As shown in Fig. 1a and b, the SEM images of BC6 shows that it appeared to be porous and has relatively maintained the original structure of the burlap fiber. The particles are large and kept their ordered shape after the pyrolysis and milling processes. On the contrary, the SEM images of GB12 (Fig. 1c and d) show that it has uniform particle distributions throughout and is obviously smaller in size.

Nanoscopic structures of the BC6 and GB12 biocarbon materials were investigated using TEM and HRTEM techniques and the obtained images are shown in Fig. 1(e)–(h). The high-resolution images indicated the presence of nanoparticles and sheets of graphene layers along the edge of the carbon phases. The dark and dense masses in the TEM images of Fig. 1e (circled with red dots) are approximately 600 nm and the dark spots in the TEM images of Fig. 1g, which represent individual particles of GB12, are less than 100 nm. These nanoparticles are widely dispersed throughout the lighter carbon structures in the TEM images. The HRTEM images of BC6 show contaminated regions possibly from the defect-rich amorphous carbon (sp^3) and other impurities in the sample (Fig. 1f, inset), which is in good agreement with previously reported observations by Lin *et al.*[25] Unlike BC6, the HRTEM image of the catalyzed burlap carbon (GB12) contains a few (3 to 12) and clean layers of graphene sheets as shown in Fig. 1h.

3.2.2. BET surface areas and pore size distributions of biocarbons. Fig. 1(i)–(k) shows the nitrogen adsorption isotherm and pore size distribution of the two burlap carbons produced at 600 °C (BC6) and 1200 °C (GB12). The BET surface area of BC6 was calculated to be 32 $m^2 g^{-1}$, but then reduced to 18 $m^2 g^{-1}$ for GB12. The internal structure of the biocarbon could be collapsed with temperature, clogging the pores to reduce the surface area of the sample.[26,27] The BC6 isotherm (Fig. 1i) showed a progressive rise with relative pressure, which is the case for biocarbons dominated by mesopores >2 nm in size, while GB12 shows a constant adsorption isotherm throughout, indicating a higher proportion of micropores in the sample.[28,29] The pore size distribution and cumulative pore volumes are provided in Fig. 1i and j. BC6 (Fig. 1i) has a high proportion of mesopores and shows apparent variations in the pore size distributions between 2 nm and 18 nm. GB12, on the other hand, has fewer variations in the pore size distributions with its maximum pore width located at around 2 nm. Smaller pore sizes are advantageous for improved conductivity because they have less voids in them.[10,30]

3.2.3. Raman analysis. Raman analysis is another powerful tool used to study the level of graphitization in carbon materials and the spectra of BC6, GB12 and CG are given in Fig. S2 (ESI†). Generally, the level of graphitization is indicated by the intensity ratio of the D-to-G peaks in the Gauss fitted Raman spectra. A lower D-to-G ratio represents a high graphitic level.[31] The Raman spectrum of each biocarbon ranging between 1000 cm^{-1} and 2000 cm^{-1} was fitted with four Gauss distribution functions as shown in Fig. 2(a) and (b). Curve fitting is used to separate multiple overlapping peaks into their individual contributions, thus providing the basis for quantitative analysis and comparison of various properties of different samples including graphene content and crystallinity. The D peak called the disorder peak appears at around 1350 cm^{-1} and is caused by the vibrations of defect (sp^3 bonded) carbons in the structure, while a perfectly crystalline carbon produces the G peak, also called the graphene peak, at around 1650 cm^{-1} due to the vibrations of sp^2 bonded carbons.[32] A significant difference in the D-to-G ratio was observed between GB12 and BC6 burlap carbons. The D-to-G ratios of the samples were calculated from the intensities of the Gauss fitted D and G peaks and

Table 1 Carbon, hydrogen, nitrogen and oxygen results of the different carbon materials

Sample	C (%)	H (%)	N (%)	O[a] (%)	Fe (%)	H/C	O/C
BC6	63	5	0.8	31.2	0.053	7.9×10^{-2}	5.0×10^{-1}
GB12	93	0.04	0.5	6.5	0.14	4.3×10^{-4}	6.9×10^{-2}
SP	94	0.09	0.09	5.8	—	1.0×10^{-3}	6.2×10^{-2}
CG	91	0.17	0.5	8.3	—	1.9×10^{-3}	9.2×10^{-2}

[a] Oxygen by difference.

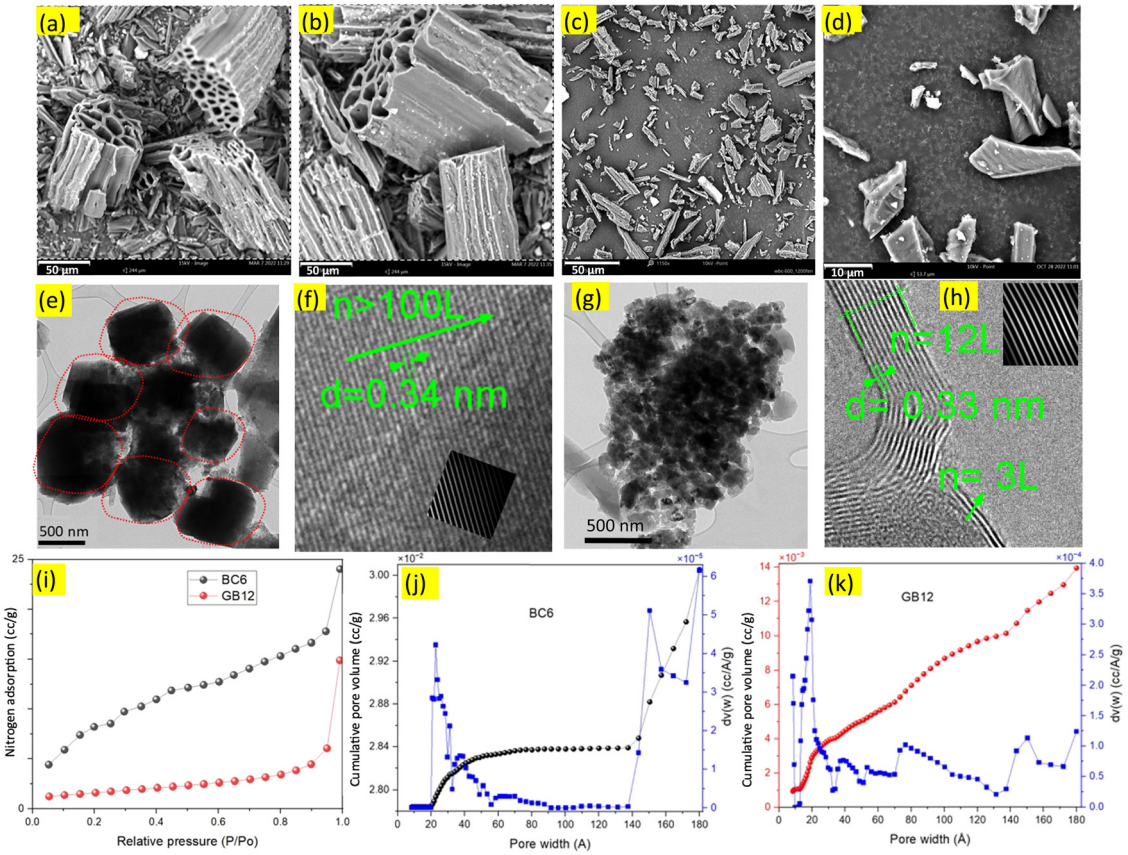

Fig. 1 SEM, TEM, HRTEM images and nitrogen adsorption plots of the burlap-based carbons produced with/without the iron nitrate catalyst. (a)–(d), SEM images of the burlap carbons. (e) and (g), TEM images showing the biocarbon nanostructures, (f) and (h) HRTEM images showing numbers (*n*) of graphene layers (L) and the interplanar spacing between the layers in nanometres. Extended HRTEM images of BC6 and GB12 are given in Fig. S4 (ESI†). For (a), (b), (e) and (f), the biocarbon was produced at 600 °C; for (c) and (d) (scale bar 10 µm), (g) and (h), the biocarbon was produced using the iron nitrate catalyst at 1200 °C. The inset in (f) is the graphene lattice showing contaminated layers. Biocarbon produced at higher temperatures shows clean, and continuous graphene layers ((h), inset) manifesting a high degree of graphitic carbons compared to the uncatalyzed burlap carbon (BC6). (i)–(k), nitrogen adsorption analysis. (i), BET surface area isotherms for the burlap-driven biocarbons generated at 600 °C (BC6) and 1200 °C using the iron nitrate catalyst (GB12). (j) Pore size and pore size distributions of the biocarbon produced at 600 °C (BC6) showing significant variations with pressure. (k), Pore size and pore size distributions of the biocarbon produced at 1200 °C, showing relatively consistent distributions throughout. Smaller and uniform pores in GB12 can form ordered and highly packed carbon, improving the packing efficiency when compressed. Reduction in the particle size of GB12 is attributed to the effective removal of oxygen and hydrogen as observed in the CHNS analysis, leading to the efficient carbon stacking process, which can result in better conductivity.

found to be 0.94 and 0.6 for BC6 and GB12, respectively, which indicate that GB12 has a better graphene content than BC6.

GB12 has a relatively sharp peak at around 2700 cm^{-1} (Fig. S2, ESI†), indicating the presence of a few layers of graphene sheets as compared to BC6. The broad bands at around 1200 cm^{-1} in (BC6) and 1340 cm^{-1} in (GB12) represent C–H in aromatic rings and sp^3 of hexagonal diamond carbon.[33] BC6 has a relatively big peak at around 1540 cm^{-1}. This peak is related to the amorphous carbon structure in the sample.[34] In contrast, the corresponding peak for GB12 exhibits a lower peak intensity, indicating a comparatively lower presence of amorphous carbon in (GB12).

3.2.4. Crystallographic properties: XRD analysis. The nature of graphitization of the biocarbon was further evaluated by the powder X-ray diffraction analysis and the obtained XRD patterns for the biocarbons (BC6 and GB12) are shown in Fig. 2c. The biocarbon produced at 600 °C revealed almost no diffraction peaks at the graphitic theta angles, which is consistent with an amorphous carbon framework,[9] while the catalyzed biocarbon (GB12) showed a noticeable XRD peak at a 2θ value of around 26°. This peak is assigned to the (002) diffractions of the graphitic carbons revealing the formation of graphitic carbons with increasing temperature in the presence of the iron nitrate catalyst, similar to the observation reported by Zhai *et al.*[36] The Raman spectra of GB12 too exhibited a smaller D-to-G ratio (Fig. 2b), implying apparent improvements in the degree of graphitization in GB12, possibly due to the growth of thin-walled graphitic shells.[35] BC6 has a sharp peak at 29.3°, which could be associated with inorganic components possibly metals within the biocarbon structures[37] and eventually disappeared in the higher temperature biocarbon (GB12). Most metals tend to evaporate from their solid matrix with increasing pyrolysis temperature. Metals including Cd, Pb, As and Zn were reported to display high volatility at such high pyrolysis temperatures.[38] However, additional investigation is recommended to precisely identify the specific metal components in the samples. The small

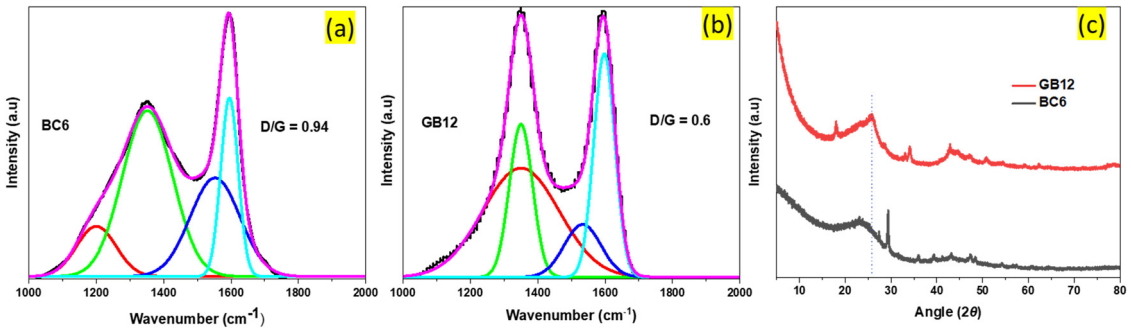

Fig. 2 Raman and XRD spectral analysis. (a) and (b), Raman spectra of the burlap-based carbon produced at 600 °C (BC6) and at 1200 °C with the iron nitrate catalyst (GB12), fitted to the Gauss distribution. The lower D-to-G ratio in GB12 is due to the reduced oxygenated groups such as the polyaromatic structures, indicating its better graphitic nature than BC6.[9] The XRD peak of GB12 (c) is broad unlike the sharp peaks commonly observed with commercial grade graphene, possibly due to the formation of ultrathin graphitic nanostructures which are hardly detected by XRD.[35]

peak at around $2\theta = 18^{\circ}$ for GB12 should be due to the formation of nanocrystallites of carbon at higher temperatures.[39,40]

3.3. Conductivity studies

The electrical conductivity of biocarbon materials is one of the key properties to diversify their application potential. Hence, the electrical conductivities of the biocarbon materials BC6 and GB12 were investigated against varying pressure and the obtained conductivity data are shown in Fig. 3. In addition, the electrical conductivities of the commercial carbon black (SP) and graphene are also presented for comparison. The values represent the averages of three repeated experiments with results not varying by more than 3%. Electrical conductivities of all the carbon powders increased with increasing compression, indicating the transitions from low to highly conductive materials. The graphitized biocarbon (GB12) showed the highest electrical conductivity ranging from 95 to 375 S m^{-1}. This conductivity value outperforms most bio-based carbons reported in numerous studies (Table 2). Given the same compression, the bulk conductivity of the graphitized biocarbon produced from waste burlap is far higher than the bulk conductivities of all carbons. The commercial grade carbon black and graphene powders have maximum conductivities of 27 S m^{-1} and 17 S m^{-1}, respectively (Fig. 3 inset).

The electrical conductivity patterns observed in this study are consistent with conductivity measurements of various biocarbons produced at similar ranges of temperature.[9,21,41] For example, the electrical conductivities of lignin-based carbons produced between 900 to 1100 °C were reported to increase from 0.2 to 1500 S m^{-1} as the packing fraction increased from 0.2 to 0.5.[47] It is worth noting that the same equipment and similar steps were followed to measure the bulk conductivity of the graphene powders as they were for the other carbon powders in this experiment. Although the graphene powder was densified to a maximum compression of 1124 kPa, it was not high enough to pack the graphene due to its agglomerated particle arrangement (Fig. S3, ESI†), which increased the electrical resistance. As a result, the commercial grade graphene (CG) was observed to have very low bulk conductivity and changes in its conductivity were negligible with compression (Fig. 3). The graphene flakes must be curled when packed forming

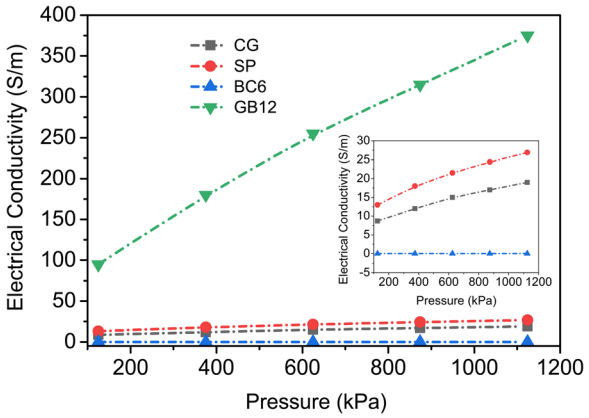

Fig. 3 Electrical conductivities of different carbons and the commercial grade graphene powder with compression. Data represent the average value of 3 repeated experiments, whose results vary less than 3%. Inset: Magnified view of electrical conductivity plots for the biocarbon produced from waste burlap at 600 °C (BC6), commercial graphene (CG) and carbon black (SP). The extremely high conductivity of GB12 is due to the presence of highly graphitized carbons in the sample.

aggregate agglomerates in addition to being disoriented, increasing the contact resistance, similar to the observation reported by Marinho *et al.*[47] In this case, particle morphology rather than graphene content has a significant impact on the bulk conductivity of the commercial grade graphene nanoplatelets.

Bigger particles with mesopore sizes as in BC6 could significantly reduce the electrical conductivity as more air could be trapped in the particle matrix. In contrast, relatively uniform particles with a high number of micropore distributions as in GB12 can effectively act as charge reservoirs and improve the conductivity.[48] The physical structure of the particles and high carbon content induced by the catalyst are among the main factors accounting for the excellent conductivity of GB12. The extremely low O/C ratio (4.3×10^{-4}) in GB12 can lead to the formation of more condensed aromatic rings with six fused rings (graphene sheets) and result in higher conductivity.[45,46] The Raman spectra of the commercial graphene (CG) show small D and high G peaks resulting in a lower D-to-G ratio (0.4) (Fig. S2, ESI†), but it has a far lower conductivity than GB12 (Fig. 3).

Table 2 Electrical conductivities of different bio-based graphitic carbons

Source of carbon	Value (S m^{-1})	Pyrolysis conditions	Ref.
Lignin	1	600–900 °C	21
Lignin	1–11	HTC at 300 °C followed by graphitization from 900–1100 °C	9
Cellulose	170	HTC at 260 °C followed by graphitization at 900 °C	11
Lignin	2–58	HTC at 130 °C followed by graphitization from 800 – 1100 °C	41
Soy hulls, light and dark roast coffee chaff	$8–10 \times 10^{-3}$	500–900 °C	42
Cellulose	10^4 (skeletal, packing density 2.2 g cm^{-3})	2000 °C	43
Birch kraft pulp	9.5×10^3 (skeletal, packing density 1.14 g cm^{-3})	1000 °C	44
Lignin	160	900 °C	28
Lignin	28	900 °C	45
Pine	350	1000 °C	46
Burlap waste	375	1200 °C	Present study

This was due to the larger spherical agglomerates of graphene (Fig. S3, ESI†), which would tend to increase the contact resistance when compressed.[47] Indeed, contact resistance has been reported to play a major role in determining the bulk conductivity of packed carbons rather than graphitic structures.[49] Carbon black (SP) used in this work is amorphous carbon without any graphene content. Its properties are extensively studied and reported in many scientific literature studies.[18,50] Its morphology (Fig. S3, ESI†) shows a fluffy structure which could also result in the formation of aggregate agglomerates during packing, leading to lower electrical conductivity.[39]

3.4. Electrochemical characterization of the capacitive cells

Capacitive cells were fabricated in pouch cell assembly using seaweed derived pristine biocarbon materials employing Super P C65 (SP), graphitised biocarbon (GB12), and Commercial Graphene (CG) as the conductive additives. A capacitive cell was also made without conductive carbon for the purpose of comparison. The cyclic voltammograms of the capacitive cells are shown in Fig. 4. The supercapacitor cells assembled using different electrode configurations showed the quasi-rectangular CV curves, which are attributed to their effective reversible reactions and indicate their capacitive performances. Although the CV curves show a similar pattern, they exhibit significant differences as shown in Fig. 6e due to the variation of conductive carbon in electrode materials. The calculated specific capacitance of the capacitive cell fabricated using the graphitised biocarbon GB12 as the conductive carbon showed the highest value of 62.5 F g^{-1}, whereas the electrodes made without conductive carbon, SP, and commercial graphene,

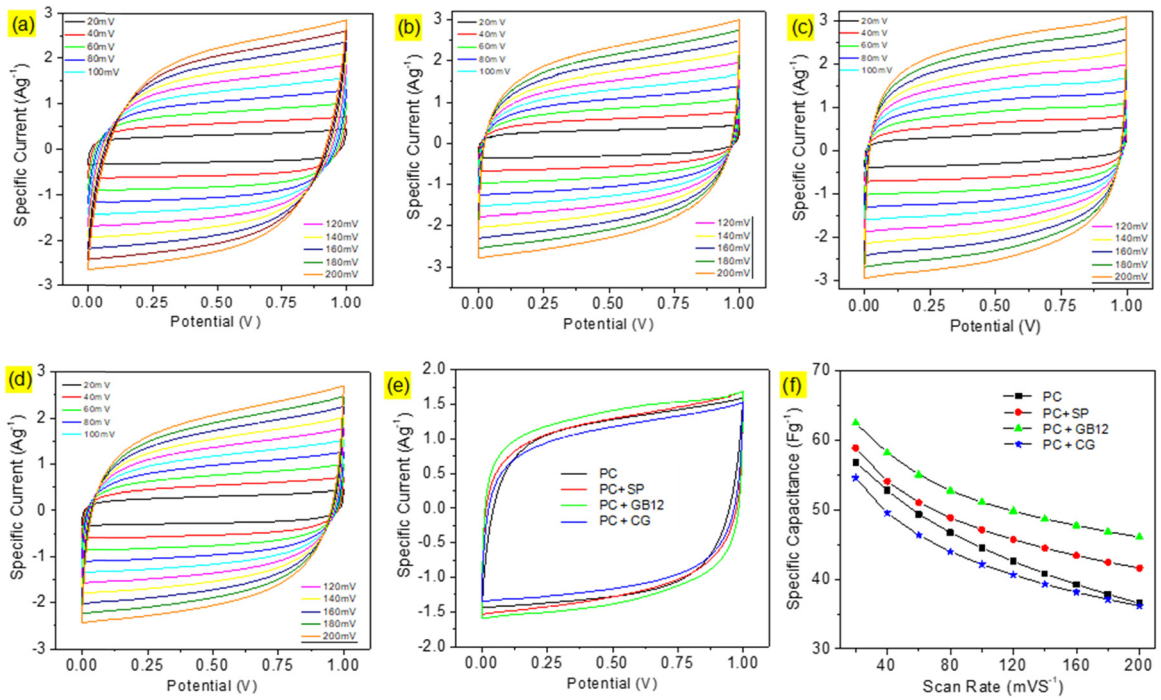

Fig. 4 Cyclic voltammograms of the supercapacitors, without conductive carbon (a), Super P C65 (b), GB12 (c), and Commercial Graphene (CG) (d) at various scan rates (20–200 mV); cyclic voltammograms of the capacitive cells at a 20 mV scan rate (e); and specific capacitance of the supercapacitors (f). The capacitive cell fabricated using the electrode with graphitised biocarbon (GB12) showed better capacitance retention, while increasing the scan rate.

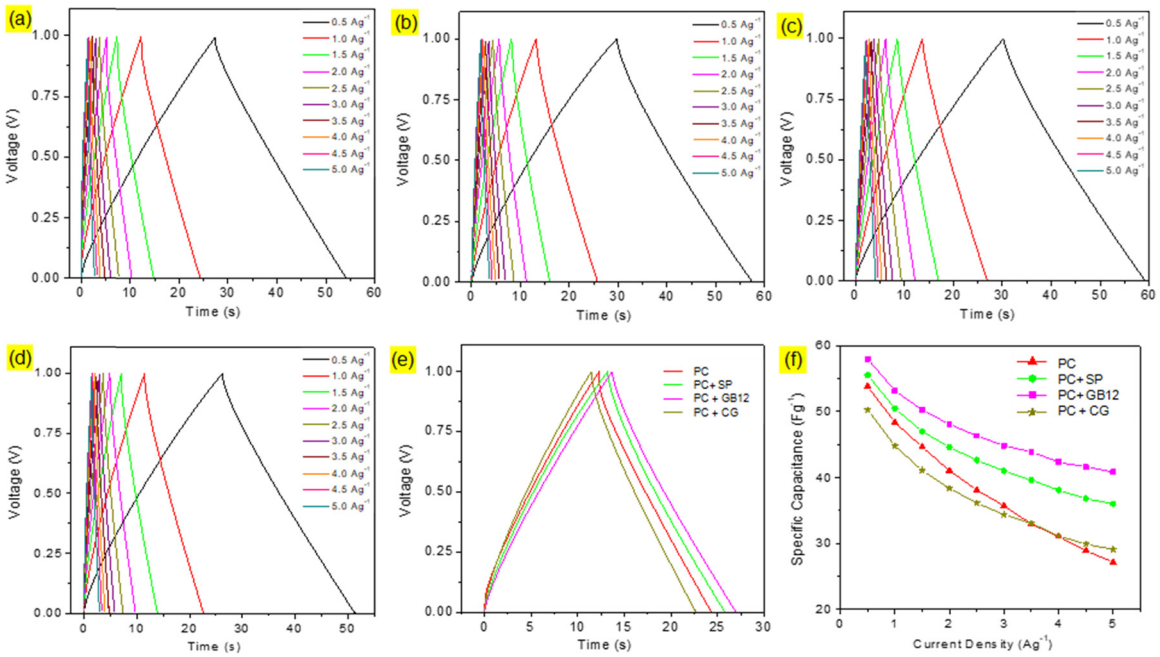

Fig. 5 Galvanostatic charge/discharge curves of the supercapacitors, without conductive carbon (a), Super P C65 (b), GB12 (c), and commercial graphene (CG) (d) at various current densities (0.5–5 A g^{-1}); GCD curves of the capacitive cells at 1 A g^{-1} current density (e); and specific capacitances of the supercapacitors (f) at various current densities (0.5–5 A g^{-1}). The electrode made of graphitised biocarbon (GB12) showed superior capacitance retention at higher current density.

respectively, showed the specific capacitances of 56.83, 58.92 and 54.58 F g^{-1} at 20 mV.

The galvanostatic charge/discharge curves of the capacitive cells showed a symmetrical triangular shape, which ensures their electrical double layer (EDL) capacitance behaviour. Their charge/discharge curves showed that the supercapacitor assembled using the electrode made of graphitised biocarbon (GB12) showed a lower IR drop compared to other cells, which is due to the lower internal resistance contributed by the highest electrical conductivity of GB12. The specific capacitances of the capacitive cells at various current densities are shown in Fig. 5f. The highest specific capacitance of 57.95 F g^{-1} at 1 A g^{-1} was observed for the electrode made of graphitised biocarbon (GB12), whereas the electrodes made without conductive carbon, SP, and commercial graphene, respectively, showed the lower specific capacitances of 53.80, 55.49 and 50.22 F g^{-1}.

Cycle performances of the supercapacitors are shown in Fig. 6a, which indicates the excellent capacitance retention of 98% over 5000 cycles at 10 A g^{-1} with the 1 M KOH electrolyte for the electrode made using the GB12 biocarbon nanostructure as the conductive carbon. The Ragone plots showed the relationship between specific energy and power densities of the capacitive cells. The supercapacitor fabricated using the GB12 biocarbon nanostructure showed the highest energy density of 2500 W h kg^{-1} at a power density of 0.25 k W kg^{-1} employing the 1 M KOH electrolyte, which is higher than the other electrodes as shown in Fig. 6b.

The Nyquist plots of supercapacitors before and after 5000 cycles are respectively shown in Fig. 6c and d. The Nyquist plots indicate the sloping line in the low frequency region and a depressed semi-circle pattern in the high-frequency region. The experimental data have been fitted as shown in Fig. 6c and d and the relevant equivalent circuit is shown in Fig. 6e. As shown in Fig. 6e, (i) R1 is the bulk resistance, (ii) C1 is the double-layer capacitance, (iii) R2 and R3 represent the charge-transfer resistance and (iv) Q1 and Q2 are constant phase elements, which are respectively assigned to double-layer and pseudo-capacitances.[51] The fitted values of R1, R2, and R3 (before and after 5000 cycles) are shown in Table 3. It was found that the internal resistance of the supercapacitors decreases while adding conductive carbons of Super P C65 (0.536 Ω), GB12 (0.464 Ω) and commercial graphene (CG) (0.698 Ω). Among these, the supercapacitor fabricated using GB12 showed the lowest resistance both before (0.464 Ω) and after (0.469 Ω) 5000 cycles, which is attributed to its highest electrical conductivity. Electrochemical studies of the fabricated supercapacitors reveal that the GB12 biocarbon nanostructure showed superior performance as the conductive carbon compared to SP, which is currently used, and commercial graphene. Lower and higher charge-transfer resistances of the capacitive cells respectively are attributed to the better and poor accessibility of electrolytes.

4. Conclusion

Waste burlap fiber was converted to highly advanced carbon nanostructures with a few layers of graphene sheets (3–12 layers) *via* two step pyrolysis at 600 °C followed by graphitization at 1200 °C in the presence of the iron nitrate catalyst. The obtained biocarbon exhibited high electrical conductivity as 375 S m^{-1}, which outperformed most biobased carbons reported

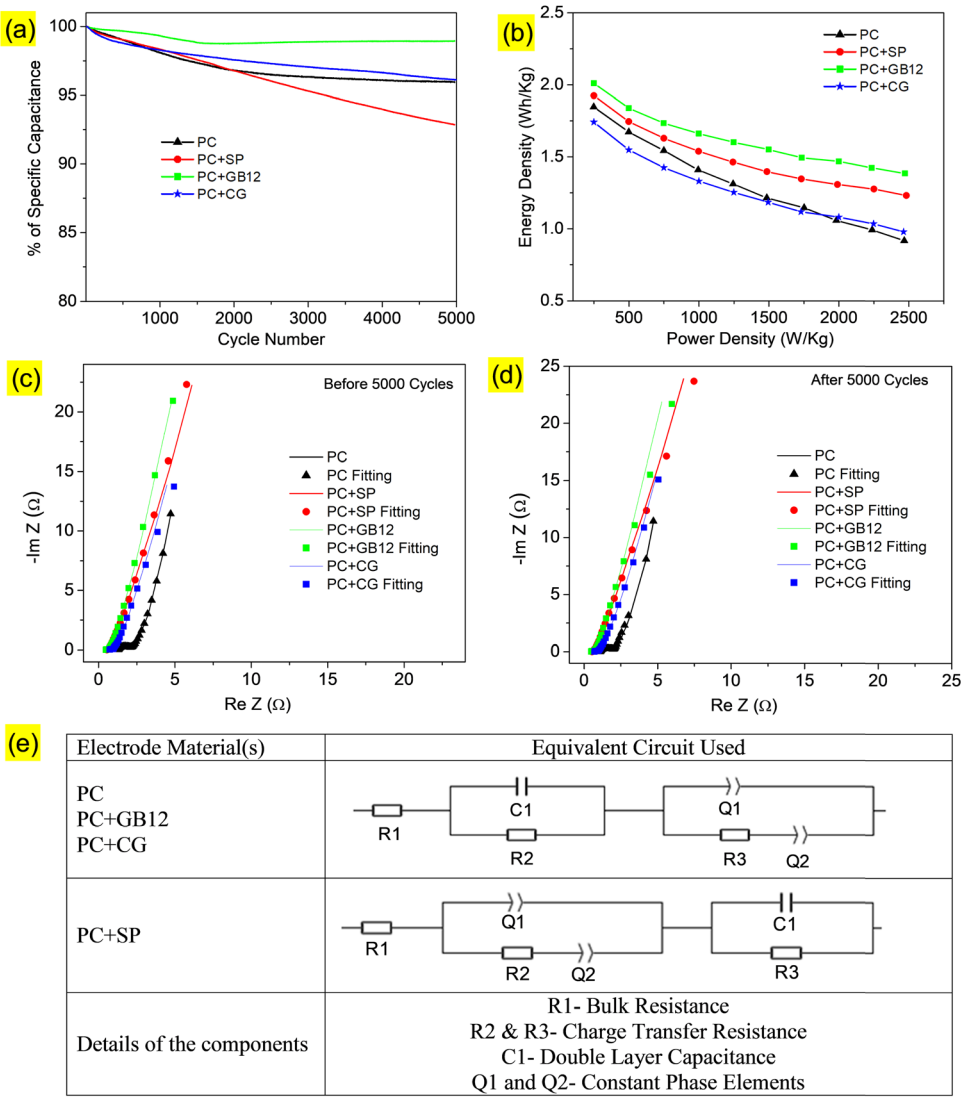

Fig. 6 Cycling stability of the supercapacitors, without conductive carbon (PC), Super P C65, GB12, and commercial graphene (CG) at a current density of 10 A g^{-1} (a); Ragone plot describing specific energy and power densities of supercapacitors (b); Nyquist plots of the supercapacitors before (c) and after 5000 cycles (d); and the equivalent circuit used to fit the impedance data (e).

in other studies. It was shown that the conductivity of biocarbon materials was governed by the physical and chemical compositions of the carbons, including graphene content and amount of oxygen, and properties such as particle morphology and distributions. Compressing the carbons resulted in the increasing conductivity of all the carbon particles and this was associated with the squashing of micropores leading to a good surface contact and reduced electrical resistance of the particles. The newly synthesized biocarbon nanostructures were successfully used as the conductive additive to sustainably substitute the commercial conductive carbon black in supercapacitor applications. Present study highlighted the potential possibility graphitised biocarbon materials in a wide range of other applications where high electrical conductivity is desired.

Table 3 Fitted values of R1, R2 and R3 before and after 5000 cycles

	Before 5000 cycles			After 5000 cycles		
Electrode	R1 (Ω)	R2 (Ω)	R3 (Ω)	R1 (Ω)	R2 (Ω)	R3 (Ω)
PC	1.279	111 783	0.816	1.090	0.200	0.740
PC+SP	0.536	0.164	0.270	0.538	0.118	0.122
PC+GB12	0.464	328.600	0.193	0.469	0.112	0.250
PC+CG	0.698	0.181	0.276	0.703	559.6	0.240

Data availability

The datasets used and/or analyzed during the current study will be available from the corresponding author on reasonable request.

Author contributions

H.W.: methodology, investigation, data curation, formal analysis, validation, visualization, writing – original draft. S.V.:

methodology, investigation, data curation, formal analysis, validation, visualization, writing – original draft. N.T.: investigation, data curation, visualization, writing – reviewing and editing. A. K. M.: conceptualization, investigation, methodology, validation, supervision, resources, funding acquisition andadministration, writing – reviewing and editing. M. M.: conceptualization, investigation, methodology, validation, resources, supervision, funding acquisition and administration, writing – reviewing and editing. All authors contributed to the discussion, reviewing, editing and approval of the manuscript for publication.

Conflicts of interest

The authors declare that they have no known conflicts of interest that could have appeared to influence the work reported in this study.

Acknowledgements

This study was financially supported by (i) the Ontario Ministry of Agriculture, Food and Rural Affairs (OMAFRA)/University of Guelph – Bioeconomy for Industrial Uses Research Program (Project No. 100038); (ii) the Natural Sciences and Engineering Research Council of Canada (NSERC), Canada Research Chair (CRC) program Project No. 460788 and the NSERC Discovery Grants Project No. 401111 and (iii) The NSERC-Collaborative Research and Development Grants (CRD) Project No. 401637 with the partner industries Prism Farms Limited and Competitive Green Technologies, Lamington, Ontario, Canada. This research has also benefited from the facility funding to the BDDC supported by FedDev Ontario; OMAFRA; Canada Foundation for Innovation (CFI); Federal Post-Secondary Institutions Strategic Investment Fund (SIF), Bank of Montreal (BMO) and University of Guelph's Alumni. Dr S. Vivekanandhan acknowledges the University Grants Commission (UGC) for providing the instrumental support through a Minor Research Project (MRP/UGC-SERO Proposal No. 1593).

References

1 D. D. L. Chung, *J. Mater. Sci.*, 2004, **39**, 2645–2661.
2 P. Murugan, R. D. Nagarajan, B. H. Shetty, M. Govindasamy and A. K. Sundramoorthy, *Nanoscale Adv.*, 2021, **3**, 6294–6309.
3 A. Devendran and A. Nagai, *Mater. Adv.*, 2023, **4**, 2524–2543.
4 D. MP, M. Misra and A. K. Mohanty, *Environ. Sci.: Adv.*, 2023, **2**, 1282–1301.
5 A. Demirbas, *Energy Sources, Part A*, 2009, **31**, 1186–1193.
6 J. S. McDonald-Wharry, M. Manley-Harris and K. L. Pickering, *Energy Fuels*, 2016, **30**, 7811–7826.
7 H. Weldekidan, V. Strezov and G. Town, *Renewable Sustainable Energy Rev.*, 2018, **88**, 184–192.
8 G. Xiao, M. Ni, R. Xiao, X. Gao and K. Cen, *J. Biobased Mater. Bioenergy*, 2012, **6**, 69–74.
9 M. Demir, Z. Kahveci, B. Aksoy, N. K. R. Palapati, A. Subramanian, H. T. Cullinan, H. M. El-Kaderi, C. T. Harris and R. B. Gupta, *Ind. Eng. Chem. Res.*, 2015, **54**, 10731–10739.
10 S. Kane, R. Ulrich, A. Harrington, N. P. Stadie and C. Ryan, *Carbon Trends*, 2021, **5**, 100088.
11 V. Hoffmann, D. Jung, J. Zimmermann, C. Rodriguez Correa, A. Elleuch, K. Halouani and A. Kruse, *Materials*, 2019, **12**, 1703.
12 T. Adinaveen, J. J. Vijaya and L. J. Kennedy, *Arabian J. Sci. Eng.*, 2016, **41**, 55–65.
13 K. Mochidzuki, F. Soutric, K. Tadokoro, M. J. Antal, M. Tóth, B. Zelei and G. Várhegyi, *Ind. Eng. Chem. Res.*, 2003, **42**, 5140–5151.
14 M. Bernardo, N. Lapa, M. Gonçalves, B. Mendes, F. Pinto, I. Fonseca and H. Lopes, *J. Hazard. Mater.*, 2012, **219–220**, 196–202.
15 Y. Yin, Q. Liu, Y. Zhao, T. Chen, J. Wang, L. Gui and C. Lu, *Energy Fuels*, 2023, **37**, 3523–3554.
16 J. Rajendran, A. N. Reshetilov and A. K. Sundramoorthy, *Mater. Adv.*, 2021, **2**, 3336–3345.
17 Z. S. Iro, C. Subramani, J. Rajendran and A. K. Sundramoorthy, *Carbon Lett.*, 2021, **31**, 1145–1153.
18 S. Kane, A. Storer, W. Xu, C. Ryan and N. P. Stadie, *ACS Sustainable Chem. Eng.*, 2022, **10**, 12226–12233.
19 C. Liedel, *ChemSusChem*, 2020, **13**, 2110–2141.
20 *X'pert Data Collector, Quick start guide, The Netherlands: version 5.3, PANalytical B.V. Almelo*; 2014.
21 M. R. Snowdon, A. K. Mohanty and M. Misra, *ACS Sustainable Chem. Eng.*, 2014, **2**, 1257–1263.
22 S. Zhang and N. Pan, *Adv. Energy Mater.*, 2015, **5**, 1401401.
23 M. D. Stoller and R. S. Ruoff, *Energy Environ. Sci.*, 2010, **3**, 1294.
24 I. N. Anyanwu, M. N. Alo, A. M. Onyekwere, J. D. Crosse, O. Nworie, C. U. Uwa and M. F. Hossain, *Data Brief*, 2018, **18**, 1064–1068.
25 L. Lin, J. Zhang, H. Su, J. Li, L. Sun, Z. Wang, F. Xu, C. Liu, S. Lopatin, Y. Zhu, K. Jia, S. Chen, D. Rui, J. Sun, R. Xue, P. Gao, N. Kang, Y. Han, H. Q. Xu, Y. Cao, K. S. Novoselov, Z. Tian, B. Ren, H. Peng and Z. Liu, *Nat. Commun.*, 2019, **10**, 1912.
26 N. Tripathi, A. Rodriguez Uribe, H. Weldekidan, M. Misra and A. K. Mohanty, *Mater. Adv.*, 2022, **3**, 9071–9082.
27 S. A. Dhar, T. U. Sakib and L. N. Hilary, *Biomass Convers. Biorefin.*, 2022, **12**, 2631–2647.
28 S. Vivekanandhan, M. Misra and A. K. Mohanty, *J. Appl. Polym. Sci.*, 2014, **132**, 41786.
29 T. T. N. Vo, S. T. Lim, J. H. Kim, G. H. Shim, K. M. Kim, B. Kweon, M. Kim, C. Y. Lee and H. S. Ahn, *RSC Adv.*, 2022, **12**, 14570–14577.
30 X. You, M. Misra, S. Gregori and A. K. Mohanty, *ACS Sustainable Chem. Eng.*, 2018, **6**, 318–324.
31 H. Weldekidan, A. K. Mohanty and M. Misra, *ACS Environ. Au*, 2022, **2**, 510–522.
32 V. Wang, D. C. Alsmeyer and R. L. Mccreery, *Chem. Mater.*, 1990, **2**, 557–563.
33 K. Maliutina, A. Tahmasebi and J. Yu, *Data Brief*, 2018, **18**, 422–431.

34 A. D. Igalavithana, S. W. Choi, J. Shang, A. Hanif, P. D. Dissanayake, D. C. W. Tsang, J.-H. Kwon, K. B. Lee and Y. S. Ok, *Sci. Total Environ*, 2020, **739**, 139845.
35 Y. Liu, Q. Liu, J. Gu, D. Kang, F. Zhou, W. Zhang, Y. Wu and D. Zhang, *Carbon*, 2013, **64**, 132–140.
36 D. Zhai, H. Du, B. Li, Y. Zhu and F. Kang, *Carbon*, 2011, **49**, 725–729.
37 A. M. Dehkhoda, N. Ellis and E. Gyenge, *J. Appl. Electrochem.*, 2014, **44**, 141–157.
38 J. He, V. Strezov, R. Kumar, H. Weldekidan, S. Jahan, B. H. Dastjerdi, X. Zhou and T. Kan, *J. Cleaner Prod.*, 2019, **234**, 1235–1245.
39 T. Ungár, J. Gubicza, G. Tichy, C. Pantea and T. W. Zerda, *Composites, Part A*, 2005, **36**, 431–436.
40 P. Kim, A. Johnson, C. W. Edmunds, M. Radosevich, F. Vogt, T. G. Rials and N. Labbé, *Energy Fuels*, 2011, **25**, 4693–4703.
41 N. K. R. Palapati, M. Demir, C. T. Harris, A. Subramanian and R. B. Gupta, in *2015 IEEE Nanotechnology Materials and Devices Conference (NMDC)*, IEEE, 2015, pp. 1–2.
42 P. Quosai, A. Anstey, A. K. Mohanty and M. Misra, *R. Soc. Open Sci.*, 2018, **5**, 171970.
43 Y.-R. Rhim, D. Zhang, D. H. Fairbrother, K. A. Wepasnick, K. J. Livi, R. J. Bodnar and D. C. Nagle, *Carbon*, 2010, **48**, 1012–1024.
44 Y. Shao, C. Guizani, P. Grosseau, D. Chaussy and D. Beneventi, *Carbon*, 2018, **129**, 357–366.
45 B. Wang, T. Shi, Y. Zhang, C. Chen, Q. Li and Y. Fan, *J. Mater. Chem. C*, 2018, **6**, 6423–6428.
46 R. Gabhi, L. Basile, D. W. Kirk, M. Giorcelli, A. Tagliaferro and C. Q. Jia, *Biochar*, 2020, **2**, 369–378.
47 B. Marinho, M. Ghislandi, E. Tkalya, C. E. Koning and G. de With, *Powder Technol.*, 2012, **221**, 351–358.
48 Z. Sun, M. Zheng, H. Hu, H. Dong, Y. Liang, Y. Xiao, B. Lei and Y. Liu, *Chem. Eng. J.*, 2018, **336**, 550–561.
49 M. Ghislandi, E. Tkalya, B. Marinho, C. E. Koning and G. De With, *Composites, Part A*, 2013, **53**, 145–151.
50 X. Zhu, F. Meng, Q. Zhang, L. Xue, H. Zhu, S. Lan, Q. Liu, J. Zhao, Y. Zhuang, Q. Guo, B. Liu, L. Gu, X. Lu, Y. Ren and H. Xia, *Nat. Sustainability*, 2020, **4**, 392–401.
51 S. Breitenbach, A. Lumetzberger, M. A. Hobisch, C. Unterweger, S. Spirk, D. Stifter, C. Fürst and A. W. Hassel, *C*, 2020 **6**, 17.